J Mater Sci: Mater Electron (2025) 36:400

Effect of doping of divalent (Cu^{2+}) and trivalent (Gd^{3+}) metal ions on microstructural and magnetic features of Mn–Zn spinel ferrite nanoparticles

Bhaurao R. Balbudhe[1], Dilip S. Badwaik[2,*], Rupesh S. Wandhare[3], Shrikant M. Suryawanshi[2], Sarang R. Daf[4], and Atul N. Yerpude[5,*]

[1] Department of Physics, Shri Dnyanesh Mahavidyalaya, Nawargaon 441223, India
[2] Department of Physics, Kamla Nehru Mahavidyalaya, Nagpur 440024, India
[3] Department of Physics, Arts, Commerce & Science College, Maregaon 445303, India
[4] Department of Physics, Shri Shivaji Science College, Nagpur 440012, India
[5] Department of Physics, Nevjabai Hitkarini College, Bramhapuri 441206, India

Received: 30 December 2024
Accepted: 19 February 2025

ABSTRACT

Two series of spinel ferrite nanoparticles $Mn_{0.5}Zn_{0.5-x}Cu_xFe_{2-y}O_4Gd_y$ (where $x = 0$, 0.05, 0.1, 0.15, 0.2, 0.25, $y = 0$, 0.1) synthesized using the co-precipitation method. The techniques of XRD, FTIR, SEM–EDS, TEM-SAED, and VSM were employed to investigate the microstructural, optical, morphological and magnetic properties of the nanoparticles. The XRD findings validated the establishment of a cubic spinel ferrite structure (Fd-3m space group). Crystallite size for Gd^{3+} substituted NPs was in the range of 15–24 nm and for without Gd^{3+} NPs 15–22 nm with varying Copper concentration. The characteristic absorption bands within the range of 400–4000 cm^{-1} associated with spinel ferrite were detected using the FTIR technique. SEM examination confirmed that the ferrite particle grains are agglomerated. EDS spectra verified the presence of all included components in the composition. Morphology & size analysis was made by TEM-SAED technique where particles shown nearly spherical shape. The measured mean particle size obtained from TEM corresponds with the crystallite size calculated from XRD data. The M–H hysteresis curve was utilized to compute and evaluate the magnetic properties of nanoparticles. The saturation magnetization (M_s), coercivity (H_c), remanence (M_r), and magnetic moment, in connection to structural and microstructural characteristics. Saturation magnetization varied when the concentration of Cu^{2+} increased, from 7.1 to 43.9 emu/g for Gd^{3+} substituted samples and 4.1 to 31.32 emu/g for Gd^{3+} unsubstituted samples. The measured value of H_c is rather low, suggesting that it can be quickly demagnetized and is suitable for electromagnetic applications.

Address correspondence to E-mail: badwaik_ds@rediffmail.com; atulyerpude@gmail.com

https://doi.org/10.1007/s10854-025-14483-x

1 Introduction

Nanoscience and nanotechnology play a crucial part in the advancement of technology in the current era of science and technology. Because of their unique properties at the nanoscale, nanomaterials are crucial to the advancement of science across many different fields. Nanoparticles are particles with a size range of 1 nm to 100 nm that are utilized to tackle technological and environmental issues in almost every field. Nanomaterials are better at mechanical, electrical, optical, and catalytic processes than their bulk equivalents. They are therefore useful for creating high-performance materials for electronics, energy storage devices, and other devices [1–4].

In recent years, magnetic nanoparticles have drawn more attention on both the scientific and academic fronts. They have been seen to have intriguing and notably distinct magnetic characteristics when compared to bulk materials. This is attributed to their larger surface-to-volume ratio [5]. Since Spinel ferrite magnetic nanoparticles have excellent coercivity and magnetic stability, they are well-known within the nanomaterial category for their use in magnetic recording media, magnetic tapes, microwave devices, and magnetic sensors. Additionally, it expands its use in biological applications like as drug delivery systems, magnetic resonance imaging (MRI), and magnetic hyperthermia for the treatment of cancer [6]. Ferrite is a class of composite magnetic material having ferrimagnetic properties. The genuine form of ferrite known as loadstone is magnetite (Fe_3O_4) [7]. There are four different types of crystal structures: hexagonal, orthoferrite, garnet, and spinel. Each has a specific application due to its particular magnetic and structural properties. Spinel ferrites are unique among these ferrites because of their high saturation magnetization, coercivity, initial permeability, minimal eddy current loss, and good dielectric qualities. And due to this, it finds a wide range of applicability in the fields discussed earlier. It has general formula AB_2O_4, where A and B represents divalent (Mn^{2+}, Zn^{2+}, Cu^{2+}, Ni^{2+}, Mg^{2+}) & trivalent (Fe^{3+}, Al^{3+} Cr^{3+}, etc.) metal ions [8]. We refer to a substance as mixed spinel ferrite when more than one divalent ion is substituted.

Among these mixed spinel ferrites, Mn–Zn ferrites are used extensively in the telecom sector over a wide frequency range because of their high permeability, strong chemical stability, and little losses. Such mixed ferrites vary in physicochemical and magnetic properties when rare earth ions are introduced. Ferrites' structural parameters, electrical properties, dielectric response, and magnetic behavior are also influenced by preparation methods, chemical makeup, doping concentration, sintering temperature, and sintering time [9]. The effects of replacing rare earth ions on the magnetic and structural properties of spinel ferrites have been extensively studied.

Zhong et al. [10], studied effects of rare earth ion (Sm, Gd, Ce, Y) doping on the structure and magnetic properties of Mn–Zn ferrites. The introduction of Gd and Sm ions reduced grain size and improved microstructure uniformity, leading to enhanced permeability and reduced coercivity at optimal doping levels (0.01 wt% for Gd/Sm and 0.03 wt% for Ce/Y). Increased doping beyond optimal levels caused non-uniform grain sizes, which negatively impacted magnetic properties, highlighting the delicate balance required in doping concentrations. Torkian et al. [11], investigated properties of Gd-doped Mn–Zn ferrites and highlighted the potential of Gd^{3+} ions to enhance magnetic properties due to their higher magnetic moment compared to Fe^{3+} ions, while also noting the variability in previous findings regarding Gd-substitution effects. Tanbir et al. [12], studied Gd-doped Mn–Zn Nano ferrites and concluded that doping with Gd^{3+} ions influences microstructural and physical properties, enhancing superparamagnetic behavior and altering the magnetic ordering at low temperatures.

Thakur et al. [13] prepared Gd^{3+} doped Mn–Zn soft ferrite nanoparticle and suggested that Gd-doped Mn–Zn ferrite nanoparticles have significant potential for biomedical applications, including targeted drug delivery and magnetic resonance imaging (MRI) contrast enhancement. Islam et al. [14] studied effect Gd^{3+} ion in Mn–Zn ferrites and concluded that Gd-substitution in Mn–Zn ferrites leads to increased lattice parameters, decreased grain sizes, and lower Curie temperatures, confirming the influence of Gd on structural and magnetic properties. Brusentsova et al. [15], synthesized Gd-substituted Mn–Zn ferrite nanoparticles and investigated their magnetic properties, particularly aiming to reduce the Curie temperature (T_C) to a range suitable for magnetic fluid hyperthermia (MFH) in cancer therapy. The study identified specific samples that demonstrated a sufficiently low T_C, making them potential candidates for MFH applications. Shrivastava, Anjali et al. [16] studied Gd doping enhances the structural and magnetic properties of Mn–Zn ferrite nanoparticles, resulting in ultra-fine particles with improved saturation magnetization.

In addition, with Gd-substituted Mn–Zn NPs are studied by varying copper concentration. Sharma et al. [17], studied Copper substituted Mn–Zn magnetic Nano ferrite. Abu-Elsaad and Nawara [18] studied an effect of Cu-concentration on Mn–Zn ferrites prepared by citrate process. The addition of copper (Cu) as a dopant increased the magnetic characteristics of manganese-zinc Nano ferrites. Effect of Cu substitution altered structural, magnetic and elastic properties of $Mn_{0.5}Zn_{0.5-x}Cu_xFe_2O_4$ studied by Alam et al. [19]. Suneetha et al. [20] investigated $Mn_{0.5-x}Cu_xZn_{0.5}Fe_2O_4$ ferrite NPs to study the role of Cu in modifying Magnetic structural properties and indicated the possibility of using them in high-frequency regions.

Summarizing the literature reported earlier, incorporation of Gd^{+3} in Mn–Zn spinel ferrite leads to enhancing superparamagnetic behavior which is significant potential for various lifesaving biomedical applications. Doping rare earth also improves magnetic anisotropy, affects coercivity and saturation magnetization which makes material suitable for magnetic storage applications. While incorporation of Cu^{+2} leads to alter structural, morphological as well as magnetic properties due to exchange interactions which is useful in high-frequency region operating devices. Doping of Cu^{+2} or any divalent ion also influences cation distribution between tetrahedral and octahedral sites which in turn improve the magnetic properties. Hence, the doping of Cu^{2+} and Gd^{3+} in the Mn–Zn spinel ferrite structure may enables precise tuning of its structural and magnetic properties for specific applications. In this research article, we have incorporated Cu^{2+} and Gd^{3+} into the Mn–Zn spinel ferrite structure and reported their combined effects.

The current study examines the effects of gadolinium (Gd) and copper (Cu) ion doping on manganese-zinc ferrite nanoparticles ($Mn_{0.5}Zn_{0.5-x}Cu_xFe_{2-y}O_4Gd_y$, $x = 0.00$, 0.05, 0.1, 0.15, 0.2, 0.25, $y = 0$, 0.1) in detail. Mn–Zn ferrites, show good magnetic properties and the effect of doping the rare earth element will improve magnetic properties; however, the effect of co-doping of copper (Cu) and gadolinium (Gd) on magnetic properties of Mn–Zn ferrites has rarely been studied so far.

2 Experimental work

2.1 Synthesis of $Mn_{0.5}Zn_{0.5-x}Cu_xFe_{2-y}O_4Gd_y$ nanoparticles

Copper and Gadolinium co-doped $Mn_{0.5}Zn_{0.5-x}Cu_xFe_{2-y}O_4Gd_y$ (where, $x = 0.00$, 0.05, 0.1, 0.15, 0.2, 0.25 $y = 0$, 0.1) spinel ferrite nanoparticles synthesized using chemical co-precipitation process. These two series of six samples each (6 substituted by Gd & 6 without Gd) prepared by varying Cu-concentration. An AR grade Manganese (II) chloride ($MnCl_2$, Alfa Aesar, 97%, USA), Zinc chloride dry ($ZnCl_2$, Alfa Aesar, 97%, USA), Ferric (III) chloride anhydrous ($FeCl_3$, Alfa Aesar, 98%, USA), Copper (II) Chloride anhydrous ($CuCl_2$, Alfa Aesar, 98%, USA), Gadolinium (III) Chloride hexahydrate ($GdCl_3.6H_2O$, Alfa Aesar, 99.9%, USA) were used as initial materials for preparation. In a first step the precursors dissolved and mixed properly (Mn–Zn–Cu and Fe–Gd separately in two beakers) in de-ionized water using magnetic stirrer for 30 min. Both solutions (Mn–Zn–Cu and Fe–Gd) then mixed and stirred for the homogeneous mixture of precursors and Temp. of solution maintained at 80 °C. By adding NaOH solution dropwise, the pH of the solutions was kept between 11 and 12. After heating, the mixture was let to cool and allow the precipitate to settle. Filtered precipitate washed with ethanol and distil water several times. The wet precipitate dried in oven and grinded for 2 h using pestle mortar. Obtained material poured in crucible and placed in the furnace to undergo calcination at 800° C for 5 Hrs. To create fine nanoparticles, samples were crushed one more time after the crucibles were taken out of the furnace. In this way the procedure is followed to synthesize all the samples. In the following discussion of this research, all Gd^{3+}($y = 0.1$) substituted with varying Cu^{2+} concentration $x = 0.00$, 0.05, 0.1, 0.15, 0.2, 0.25 samples will be denoted as B-1 to B-6 and samples without Gd^{3+} ($y = 0$) with varying Cu^{2+} concentration $x = 0.00$, 0.05, 0.1, 0.15, 0.2, 0.25 will be denoted as B-7 to B-12.

2.2 Characterization techniques

All material's XRD spectra were obtained using X-ray diffractometer (Model-Rigaku Mini-Flex 600) in the 2θ range of 20° to 80° using CuKα radiation ($\lambda = 1.54059$ Å). Fourier Transform Infrared spectroscopy (FTIR) was utilized to investigate the functional group between 450 and 4000 cm^{-1} utilizing model: PerkinElmer Spectrum-2 FTIR Spectrometer. The surface appearances and compositional analysis of NPs were examined using a scanning electron microscope (Model-Jeol 6390LA with EDAX facility). Transmission electron microscopy (TEM with SAED) examined the microstructure using JEOL JEM-1400. Room temperature magnetic properties of synthesized spinel ferrite nanoparticles were obtained via Vibrating Sample Magnetometer (VSM) of the Lakeshore 7400S series. The experimental approach consisted the use of a magnetic field ranging from − 20,000 to + 20,000 Oe.

3 Results and discussion

3.1 XRD Studies

To study the crystalline nature of $Mn_{0.5}Zn_{0.5-x}Cu_xFe_{2-y}O_4Gd_y$ nanoparticles X-ray diffraction data are obtained. Figure 1a, b reveals the patterns

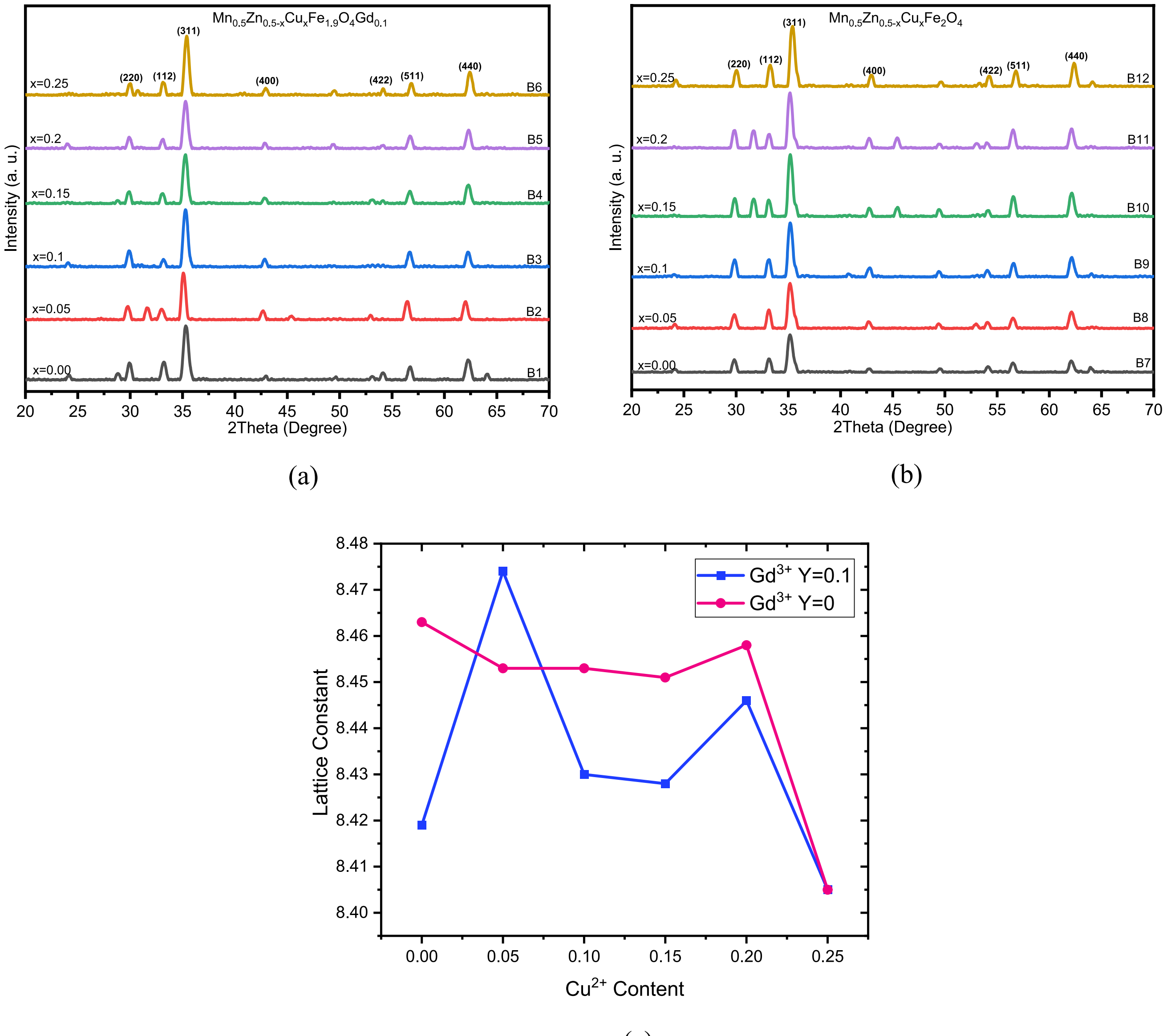

(a) (b)

(c)

Fig. 1 **A** XRD pattern of $Mn_{0.5}Zn_{0.5-x}Cu_xFe_{1.9}O_4Gd_{0.1}$ for $x = 0.00, 0.05, 0.1, 0.15, 0.2, 0.25$. **b** XRD pattern of $Mn_{0.5}Zn_{0.5-x}Cu_xFe_2O_4$ for $x = 0.00, 0.05, 0.1, 0.15, 0.2, 0.25$. **c** Variation of Lattice constant with Cu^{2+} content for Gd^{3+} substituted & unsubstituted samples of XRD data of produced NPs. The characteristic diffraction peaks seen at various angles with the miller indices (220), (112), (311), (400), (422), (511) and (440) confirms cubic spinel structure and also represents Fd-3m space group of spinel phase. XRD, patterns showed the effective incorporation of Cu^{2+} & Gd^{3+} ions in Mn–Zn spinel lattice. Crystalline size for all samples calculated using full width half maxima of prominent peak (311) and found to be varying with Cu^{2+} and Gd^{3+} concentration accordingly. Equation (1) used to evaluate crystalline size is (Debye-Scherer's Formula),

$$D_{\mathrm{XRD}} = \frac{k\lambda}{\beta\cos\theta}, \quad (1)$$

where k is Scherrer's constant ($k = 0.9$), λ is the X-ray wavelength (0.15406 nm), θ is Bragg's diffraction angle & β be the FWHM. Obtained crystallite size for both series was found to be nearly same (15–24 nm for Gd-substituted and 15–22 nm for Gd unsubstituted).

Experimental lattice constant (a) for each sample was calculated by the relation,

$$a_{\mathrm{exp}} = \frac{\lambda}{2\sin\theta}\sqrt{h^2 + k^2 + l^2} \quad (2)$$

here λ is wavelength (0.15406 nm) and θ is Bragg's diffraction angle. Lattice constant varies as it is dependent on RE^{3+} ionic radius and the cationic distribution among the Interstitial A and B-sites of the spinel lattice [21]. Observed values are shown in Table 1. Lattice constant behaviour with increasing concentration of Cu^{2+} with and without Gd^{3+} depicted in Fig. 1c. The trend of lattice constant with Cu^{2+} concentration is found to be enhanced for samples without and with Gd-substituted samples may be due to replacement of Zn^{2+} ions by Cu^{2+} ions as ionic radius of Cu^{2+} (0.73Å) ions is less than Zn^{2+} (0.80Å) ions. Similar result is supported by the other group of researchers [19, 22]. However, a complex behaviour is observed for Gd-substituted samples (B1 to B6). It is due to replacement of Fe^{3+} by Gd^{3+} ions which has difference in their ionic radii. The minor irregularity in the fluctuation of the lattice constant suggests that Cu^{2+} and Gd^{3+} ions are randomly allocated at tetrahedral and octahedral positions.

The theoretical lattice constant calculated using the relation suggested by Mazen et al. [23],

$$a_{\mathrm{th}} = \frac{8}{3\sqrt{3}}\left[(r_{\mathrm{A}} + R_0) + \sqrt{3}(r_{\mathrm{B}} + R_0)\right], \quad (3)$$

where R_0 denotes oxygen ion radius, and r_{A} and r_B represent the ionic radii of the A- and B-sites, respectively. A close concordance between the a and a_{th} values is seen from XRD analysis. Change in induced strain also observed due to replacement of Gd with Fe and hence affected the D [24]. The unit cell volume of NPs is calculated using the relation,

$$V = a^3 \quad (4)$$

Slight variations in cell volume observed for B1 to B12 samples. The unit cell may expand or contract when Gd^{3+} cations replace Fe^{3+} cations, which will impact the micro strain values. The X-ray density for all samples calculated using the relation,

$$\rho_{\mathrm{x\text{-}ray}} = \frac{8M}{Na^3}, \quad (5)$$

Table 1 Peak position, crystallite size, calculated and theoretical lattice constant, volume, strain, dislocation density, interplanar spacing, X-ray density, experimental density and porosity of samples B1 to B12

Sample	2θ(°)	D (nm)	A (Å)	a_{th} (Å)	V (Å^3)	$\varepsilon \times 10^{-3}$	$\rho_{\mathrm{x\text{-}ray}}$ (g/cm^3)
B1	35.33	15	8.419	8.419	596	7.4	5.47
B2	35.09	24	8.474	8.474	608	4.6	5.36
B3	35.28	17	8.430	8.430	599	6.6	5.45
B4	35.29	19	8.428	8.428	598	5.9	5.45
B5	35.21	19	8.446	8.446	602	5.8	5.41
B6	35.39	18	8.405	8.405	593	6.0	5.49
B7	35.14	22	8.463	8.463	606	5.0	5.17
B8	35.18	15	8.453	8.453	604	7.2	5.18
B9	35.18	18	8.453	8.453	604	6.3	5.18
B10	35.19	23	8.451	8.451	603	4.7	5.18
B11	35.16	24	8.458	8.458	605	4.7	5.17
B12	35.39	18	8.405	8.405	593	6.0	5.26

where M is the molecular weight, N is Avogadro's number and a denote the lattice parameter. Observed value of X-ray density for Gd-substituted samples is higher than samples without Gd. Because the enhancement in lattice constant which occurred due to differences in the radius of the gadolinium and iron ion.

The microstructural parameters of Gd^{3+} & Cu^{2+} added Mn–Zn ferrite NPs such as Site radii (r_A, r_B), Bond length (d_{AX}, d_{BX}), Shared edges (d_{AXE}, d_{BXE}), Unshared edges(d_{BXEU}) evaluated using the Eqs. (6–14) and depicted in Table 2,

$$r_A = [u - 0.25]a\sqrt{3} - R_0 \tag{6}$$

$$r_B = [0.625 - u]a - R_0 \tag{7}$$

$$d_{AX} = \left(u - \frac{1}{4}\right)a\sqrt{3} \tag{8}$$

$$d_{BX} = a\left(3u^2 - \frac{11}{4}u + \frac{43}{64}\right)^{1/2} \tag{9}$$

$$\mathrm{d}_A = 0.25a\sqrt{3} \tag{10}$$

$$\mathrm{d}_B = 0.25a\sqrt{2} \tag{11}$$

$$d_{AXE} = a\sqrt{2}(2u - 0.5) \tag{12}$$

$$d_{BXE} = a\sqrt{2}(1 - 2u) \tag{13}$$

$$d_{BXEU} = a\sqrt{(4u^2 - 3u + 0.6875)}, \tag{14}$$

where a is lattice constant, u is oxygen positional constant and R_0 is oxygen anion radii (1.32 Å). Among the evaluated values, site radius for A- & B-sites observed to be decreasing for samples without Gd and increasing for samples with Gd with exception at $x = 0.25$ (B6 sample) of Cu^{2+} concentration. This reduction in respective quantities could be due to replacement of Zn^{2+} ions by Cu^{2+} ions because ionic radius of Cu^{2+} (0.73Å) ions is less than Zn^{2+} (0.80Å) ions as discussed earlier. Bond lengths of tetrahedral site (d_{AX}) and octahedral site (d_{BX}) as well as ionic radii values for A-sites and B-sites enhances as it is consistent with the observed variations in the lattice constant. In addition, with these quantities, other quantities are exclusively lattice constant dependent. Hence affected accordingly. The obtained results are consistent with previous literature [19]. Major change in structural parameters could be observed if concentration of Gd^{3+} ions increased to higher extent to replace Fe^{3+} ions.

The oxygen positioning parameter (u) was determined for all synthesized samples using the relation [25],

$$u = \left[\frac{1}{a_{th}\sqrt{3}}(R_0 + r_A) + 0.25\right] \tag{15}$$

Typical value of oxygen positional parameter (u) is 0.375. We observed value 0.384 for all synthesized samples. Similar results are observed by other researchers [12]. The precise value of u affects the distribution of cations (Mn, Zn, Fe) between tetrahedral and octahedral sites. This cation distribution is crucial

Table 2 Tetrahedral ionic radii (r_A), octahedral ionic radii (r_B), tetrahedral site radii (d_{AX}), octahedral site radii (d_{BX}), tetrahedral hopping length (d_A), octahedral hopping length (d_B), tetrahedral edge (d_{AXE}), shared octahedral edge (d_{BXE}), unshared octahedral edge (d_{BXEU}) for samples B1 to B12

Sample	r_A (Å)	r_B (Å)	d_{AX} (Å)	d_{BX} (Å)	d_A (Å)	d_B (Å)	d_{AXE} (Å)	d_{BXE} (Å)	d_{BXEU} (Å)
B1	0.634	0.709	1.954	2.031	3.645	2.976	3.190	2.762	2.980
B2	0.646	0.722	1.966	2.045	3.669	2.996	3.212	2.781	3.000
B3	0.636	0.711	1.956	2.034	3.650	2.980	3.195	2.766	2.984
B4	0.636	0.711	1.956	2.034	3.649	2.979	3.194	2.765	2.983
B5	0.640	0.715	1.960	2.038	3.657	2.986	3.201	2.771	2.990
B6	0.630	0.705	1.950	2.028	3.639	2.971	3.185	2.758	2.975
B7	0.644	0.719	1.964	2.042	3.664	2.992	3.207	2.777	2.996
B8	0.642	0.717	1.962	2.040	3.660	2.988	3.204	2.774	2.992
B9	0.642	0.717	1.962	2.040	3.660	2.988	3.204	2.774	2.992
B10	0.641	0.716	1.961	2.039	3.659	2.988	3.203	2.773	2.991
B11	0.643	0.718	1.963	2.041	3.662	2.990	3.205	2.775	2.994
B12	0.630	0.705	1.950	2.028	3.639	2.971	3.185	2.758	2.975

for determining the overall magnetic and structural behavior of Mn–Zn ferrites. The deviation of oxygen positional parameter indicated distortions in crystal structure and cationic redistribution which resulted change in structural as well as magnetic properties.

3.2 FTIR analysis

The spectra of all samples, recorded by Fourier Transform Infrared spectroscopy for functional group analysis, are displayed in Fig. 2a. All spectra were recorded in the range 400 to 4000 cm^{-1}. The solid green line in the spectra represents absorption band at tetrahedral site (ν_1) whereas magenta colored solid line indicates absorption band at octahedral site (ν_2). The significant absorption bands between 400 and 600 cm^{-1} range indicate and confirm the emergence of the spinel ferrite phase [26, 27].

The oscillations of Fe–O bonds inside a crystal lattice are crucial for comprehending material properties,

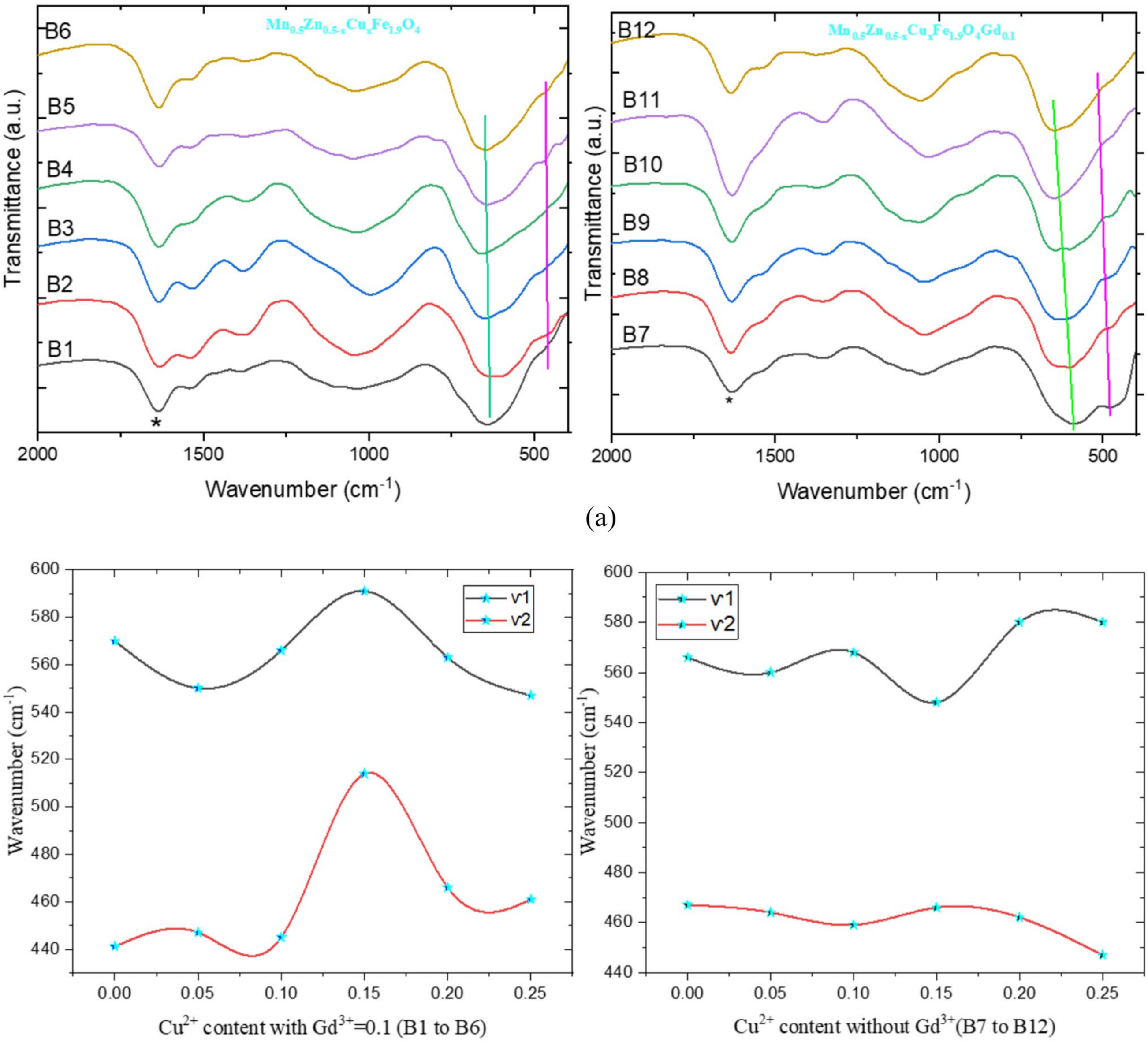

(a)

(b)

Fig. 2 **A** FTIR Spectra of $Mn_{0.5}Zn_{0.5-x}Cu_xFe_{2-y}O_4Gd_y$ ($x=0.00$, 0.05, 0.1, 0.15, 0.2, 0.25, $y=0$, 0.1). **b** Variation of ν_1 & ν_2 for B1 to B12 samples with Cu^{2+} ($x=0$, 0.05, 0.1, 0.15, 0.2, 0.25) & Gd.$^{3+}$ ($y=0$, 0.1) content. **b** EDS spectra of samples (B1, B6, B7, and B12) especially in oxides where metal ions interact with oxygen ions. In this context, the stretching vibrations manifest at both tetrahedral (A-site) and octahedral (B-site) positions. The higher frequency band (ν_1) corresponds to Fe–O stretching at tetrahedral sites, while the lower frequency band (ν_2) corresponds to those at octahedral sites. As the Cu^{2+} content increased in Gd^{3+} with & without substituted series, the synthesized ferrite NPs displayed changes in ν_1 & ν_2 values (Table 3). The variation in the M–O distances for the octahedral and tetrahedral complexes accounts for the difference in the band locations of ν_1 & ν_2 [28].

It has been noted that the ν_2 values changed towards greater wavenumber as the copper content is increased from $x = 0$ to 0.25 with $Gd^{3+} = 0.1$. Specifically, at $x = 0.15$ highest value of ν_2 is observed. The variation of ν_2 with Cu content from $x = 0$ to 0.25 with $Gd^{3+} = 0$ shown the decreasing trend. This shift in ν_2 for Gd-substituted & unsubstituted samples suggests that Gd^{3+} is occupying B-site [29]. The effect of Cu^{2+} and Gd^{3+} content on ν_1 & ν_2 values shown in Fig. 2b. In general, both (ν_1 & ν_2) values observed to be shifted to higher values for $Gd^{3+} = 0.1$ content than samples without Gd^{3+}. Our results match with those results published by Islam, R., et al. [14].

Force constant indicating the strength of intermolecular interactions, specifically the strength of the Fe–O bond at tetrahedral and octahedral sites, determined using the specified relation,

$$K = 4\pi^2\mu v^2 c^2, \tag{16}$$

where K is force constant, C is velocity of light, μ reduced mass of Fe^{3+} and O^{2-}ions v is vibrational frequency. The computed values of K_t & K_o shown in Table 3. The alteration in the bond lengths of cations and oxygen ions at the octahedral and tetrahedral sites is denoted by the values of K_o and K_t. The creation of the spinel ferrite phase in the Fd-3 m space group can be confirmed when the ratio of the force constants of the tetrahedral and octahedral sites for the unit displacement of cation–oxygen approaches 2, and the ratio of ν_1 to ν_2 is approximately 1.41. [30, 31]. We reported K_t/K_o ratio near to 1.49 for B1to B6 samples and 1.51 for B7 to B12 samples whereas ν_1/ν_2 ratio near to 1.2 for all samples. The extra absorption peak at around 1628–1633 cm^{-1} is attributed to OH group may be absorbed during coprecipitation synthesis process [32].

3.3 SEM micrograph and EDS analysis

The images collected by a scanning electron microscope were utilized to analyze the sample's morphology, dimensions, and form. Figure 3a shows SEM micrograph of samples B1, B6, B7 & B12. SEM pictures verify the existence of nanoscale particles in all samples. It is observed from XRD data that, crystalline size is varying with Cu^{2+} and Gd^{3+} concentration. According to SEM pictures, the majority of grains are observed to be agglomerated. No significant morphological difference observed for all samples. Based on the clustered and rough morphology, this image likely shows a material with a highly irregular surface or a granular structure.

The elemental composition of synthesized nanoparticles is investigated using energy dispersive X-ray spectroscopy. Energy-dispersive X-ray analysis (EDS) is an analytical method for the elemental

Table 3 Wavenumber, force constant for samples B1 TO B12

Sample	ν_1 (cm^{-1})	ν_2 (cm^{-1})	K_t (10^2N/m)	K_o (10^2N/m)	K_t/K_o	ν_1/ν_2
B1	570	441	238	142	1.6	1.2
B2	550	447	221	146	1.5	1.2
B3	566	445	234	145	1.6	1.2
B4	591	514	255	193	1.3	1.1
B5	563	466	232	159	1.4	1.2
B6	547	461	219	155	1.4	1.1
B7	566	467	234	159	1.4	1.2
B8	560	464	229	157	1.4	1.2
B9	568	459	236	154	1.5	1.2
B10	548	466	220	159	1.3	1.1
B11	580	462	246	156	1.5	1.2
B12	580	447	246	146	1.6	1.2

Fig. 3 **A** SEM images of samples (B1, B6, B7, and B12). **B** EDS Spectra of Samples (B1, B6, B7 & B12)

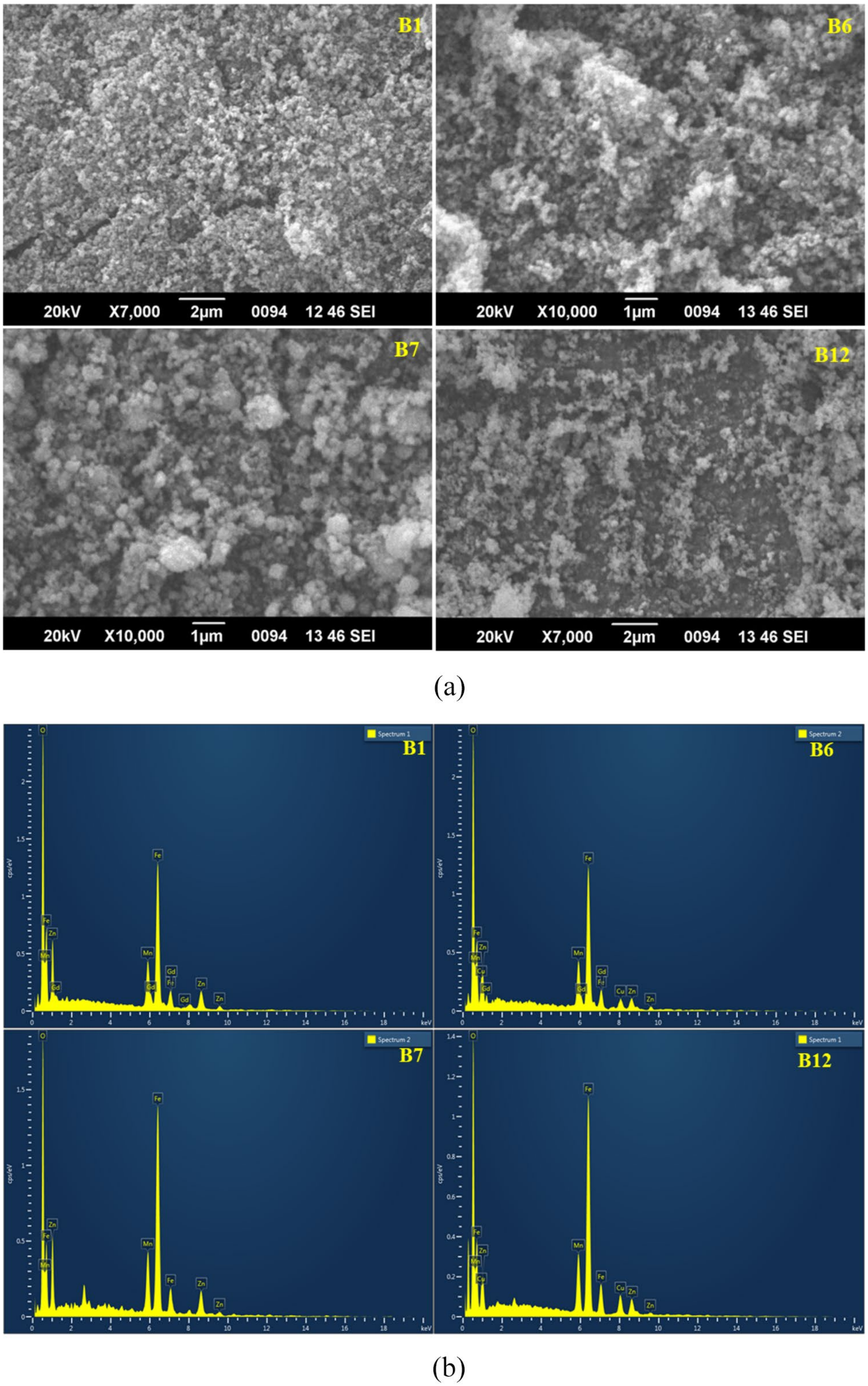

(a)

(b)

characterization of prepared materials. To verify the existence of Fe, Mn, Zn, Cu, Gd and O elements, EDS spectra were obtained for the B1, B6, B7 and B12 samples. Figure 3b indicates the EDS spectra of NPs. All elements shown their relative presence in synthesized samples as per expectancy. The obtained EDS result also indicates that, there is a successful substitution of Fe^{3+} ions by Gd^{3+} ions. The elemental wt% comparison for all elements is presented in Table 4. The starting and experimental elemental wt% matches to a greater extent. This data revealed the complete formation of spinel ferrite formation and indicates the purity of samples.

3.4 TEM analysis

A TEM imaging examination elucidates the dimensions and microstructural morphology of the synthesized nanoparticles. The morphology and size analysis of B1, B6, B7 & B12 spinel ferrite NPs are studied by the transmission electron microscope (TEM). Micrographs with their particle size distribution histograms are presented in Fig. 4a. Average particle size calculated from TEM micrographs was found to be 37.27 nm, 27.44 nm, 33.19 nm, 36.68 nm for B1, B6, B7 & B12 samples, respectively. To determine the average particle size ImageJ software is utilized. The determined mean particle size correlates with the crystalline size derived from XRD data. Presented TEM micrograph reveals presence of slight agglomerated nanoparticles with sphero-cubical structure. The agglomeration in the samples signifies robust magnetic dipole interaction among ferrite nanoparticles [33, 34]. The XRD crystallite size is often smaller than the TEM particle size because XRD only considers a single coherent crystal domain, while TEM captures entire nanoparticles, including multiple crystallites, grain boundaries, and agglomerates. Our synthesized samples have revealed polycrystalline nature from XRD analysis as well as TEM images showed agglomerated nature. In polycrystalline materials, a particle consists of multiple smaller crystallites, with crystallite size referring to the size of an individual crystal, which is often smaller than the overall particle. Hence Average particle size calculated from TEM studies shows larger value than Crystallite size observed from XRD data [35, 36].

Selected-area electron diffraction (SAED) patterns of the same samples depicted in Fig. 4b. The bright spots in the patterns depict polycrystalline nature of samples which is consistent with XRD data.

3.5 Room temperature magnetic properties (VSM)

Figure 5 illustrates the magnetic characteristics at room temperature, analyzed through the hysteresis loop of samples B1 to B12 acquired from a Vibrating Sample Magnetometer (VSM). All the samples show S-shaped curve which exhibit soft magnetic characteristics. The magnetic characteristics of spinel ferrites are predominantly influenced by the kind and concentration of substituent metal ions, together with their arrangement in the tetrahedral and octahedral positions of the spinel framework. The values of coercivity (Hc), saturation magnetization (M_s), and remanence (M_r) were derived from the VSM observations. The values obtained are displayed in Table 5. The magnetic properties of a material are affected by both intrinsic factors (like cation distribution, strain in the lattice, and lattice parameter) and external factors (including structure, density, and manufacturing method) [37].

Based on Cu^{2+} content addition with Gd^{3+} (samples B1 to B6), the value of coercivity shows (Fig. 6) increasing trend except for B3 ($x = 0.1$). Hc value increased from 11.764 to 76.303 Oe. Also, based on Cu^{2+} content addition without Gd^{3+} for Samples B7 to B12, the value of coercivity shows initially decreasing trend for $x = 0$ to 0.1 and then increasing trend for $x > 0.1$. This behaviour

Table 4 Comparison of experimental wt% with starting percentages

Element	B1 wt%		B6 wt%		B7 wt%		B12 wt%	
	Starting	Experimental	Starting	Experimental	Starting	Experimental	Starting	Experimental
O	26.01	28.54	26.06	28.58	27.13	24.45	27.18	23.22
Mn	11.1	11.16	11.18	12.14	11.64	13.08	11.66	11.12
Fe	43.13	42.12	43.21	40.67	47.35	48.19	47.44	48.21
Cu	0	0	6.47	5.16	0	0	6.74	8.75
Zn	13.28	12.5	6.65	7.38	13.8	14.28	6.94	8.71
Gd	6.39	5.67	6.40	6.07	0	0	0	0
Total%	100.00	99.99	100.00	100.00	100.00	100.00	100.00	100

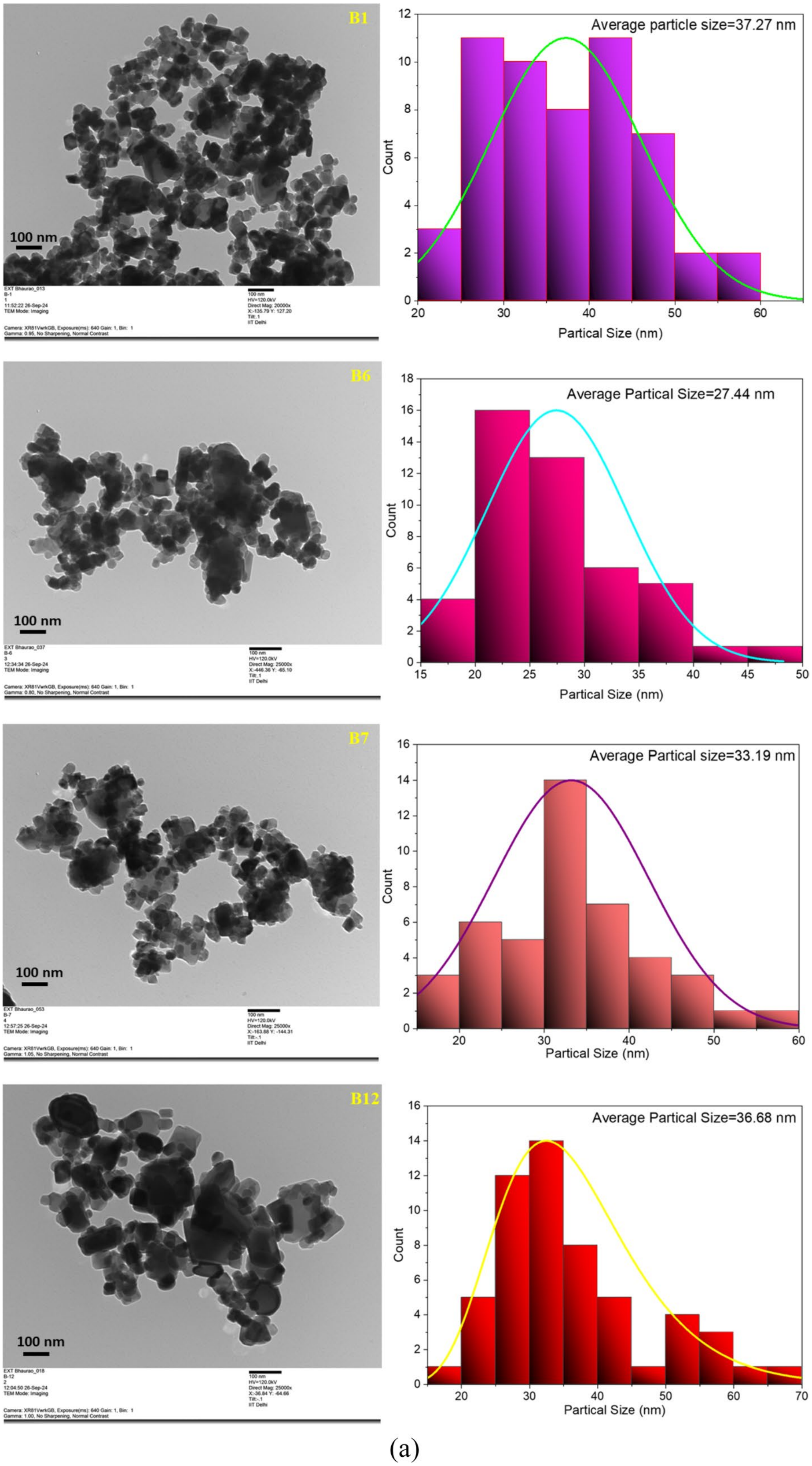

Fig. 4 **A** TEM micrograph and its Histogram revealing average particle size of B1, B6, B7 & B12 ferrite NPs. **b** SAED pattern of B1, B6, B7 & B12 ferrite NPs

Fig. 4 continued

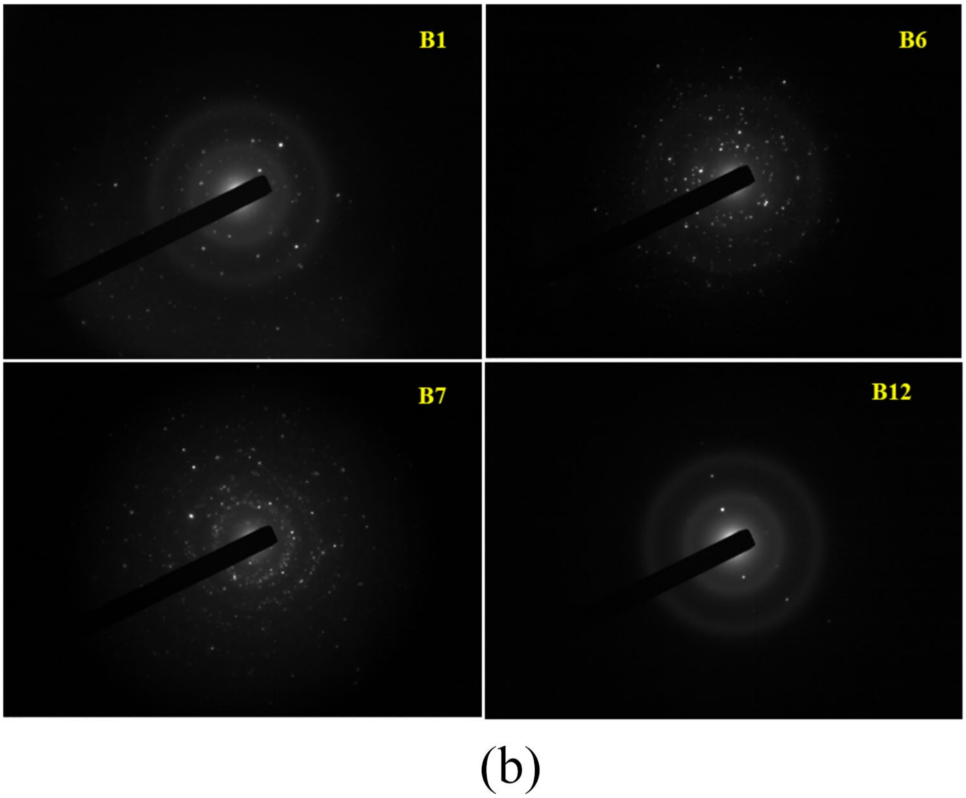

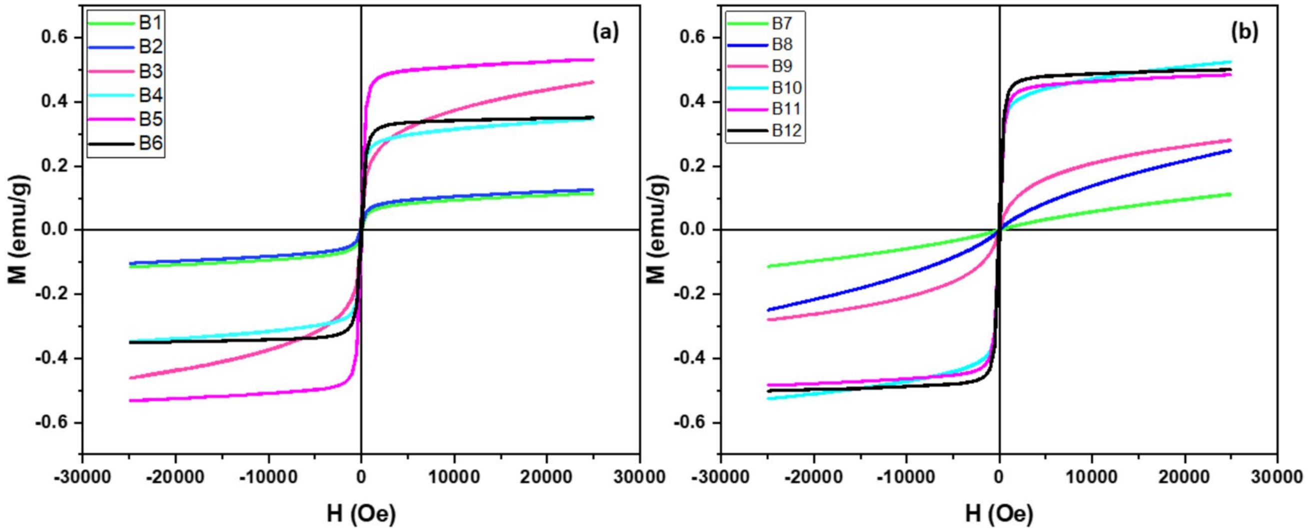

Fig. 5 M–H loops for **a** B1 to B6 samples, **b** B7 to B12 samples

could be explained using grain size & crystalline size variations. Recent study has demonstrated that several factors, including micro strain, magneto crystallinity, size distribution, magnetic domains size, and anisotropy affect the coercivity of a specific composition [38]. We have observed that crystalline size is influenced by Cu^{2+} and Gd^{3+} addition in XRD studies. Consequently, it can be stated that the coercivity of ferrites is influenced by morphology, magneto crystallinity, particle size, domain size [29]. The discovered value of *Hc* is comparably low indicating can be demagnetized easily and suited to electromagnetic applications [39]. It has been

Table 5 Saturation magnetization (M_s), Remanent magnetization (M_r), coercivity (H_c), squareness ratio (*S*), Bohr's magneton (ηB), magneto-crystalline anisotropy (*K*) for B1 to B12 Samples

Sr.No	Sample	H_c (Oe)	M_r (emu/g)	M_s (emu/g)	*K* (erg/g)	*S*	μ_B (μ_B)
1	B1	11.764	0.067	7.173	86.11	0.009	0.315
2	B2	11.768	0.032	3.4764	41.74	0.009	0.152
3	B3	5.290	0.082	20.997	113.35	0.003	0.923
4	B4	34.335	1.279	26.714	935.93	0.047	1.174
5	B5	64.358	3.295	31.315	2056.48	0.105	1.376
6	B6	76.303	5.312	43.911	3418.93	0.120	1.929
7	B7	99.1	0.032	4.17	421.68	0.007	0.176
8	B8	65.644	0.046	6.2198	416.62	0.007	0.262
9	B9	6.868	0.040	17.538	122.92	0.002	0.739
10	B10	18.113	0.540	22.833	422.00	0.023	0.962
11	B11	42.587	1.844	30.294	1316.47	0.060	1.276
12	B12	75.018	3.931	31.325	2397.89	0.125	1.319

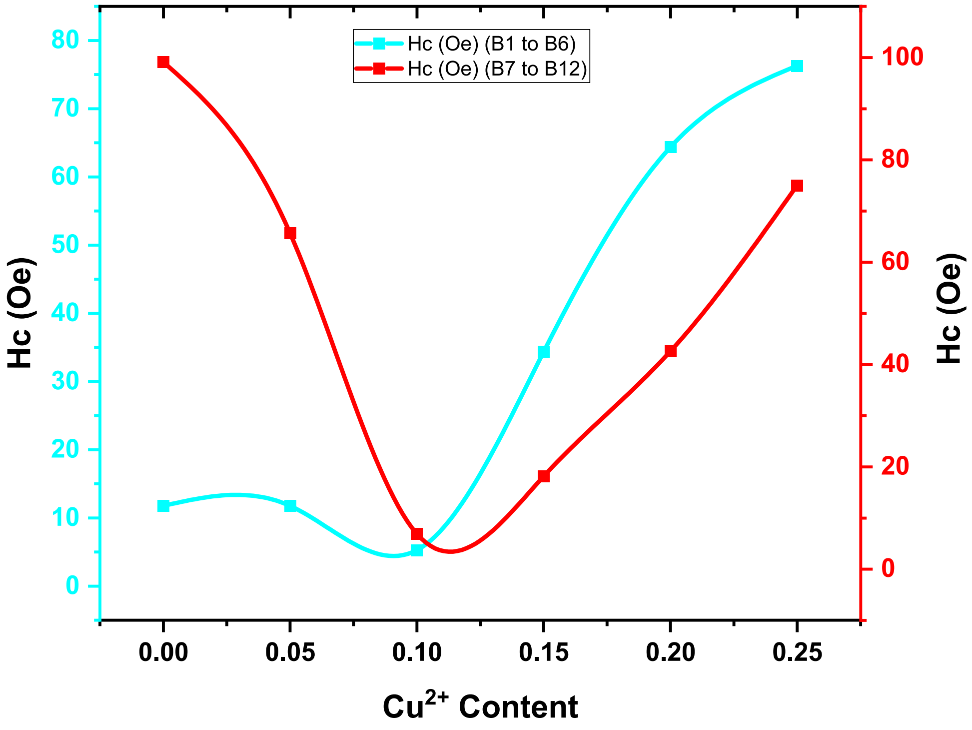

Fig. 6 Variation of Coercivity with Cu^{2+} for B1 to B6 and B7 to B12 Samples

also reported that low value of coercivity makes those nanoparticles applicable in hyperthermia applications [40]. The superparamagnetic characteristics exhibited by produced nanoparticles can also be utilized for magnetic recording [41, 42].

The magneto-crystalline anisotropy constant (*K*) is calculated using M_s and H_c values by the relation,

$$\text{Anisotropy constant } (K) = \frac{H_c \times M_s}{0.98} \tag{17}$$

It has been observed that with increment of Cu^{2+} content anisotropy constant is increased for B1 to B6 samples. And, for B7 to B12 samples anisotropy constant varied with H_c variation.

Behavior of saturation magnetization (M_s) for samples B1 to B6 & B7 to B12 shown in Fig. 7a. When the concentration of Cu^{2+} increased, saturation magnetization also increased significantly with the exception at $x = 0.05$ for B1 to B6 samples. The same trend is shown for Gd^{3+} substituted samples (B7 to B12) with increasing Cu^{2+} content. Also, we observed the same

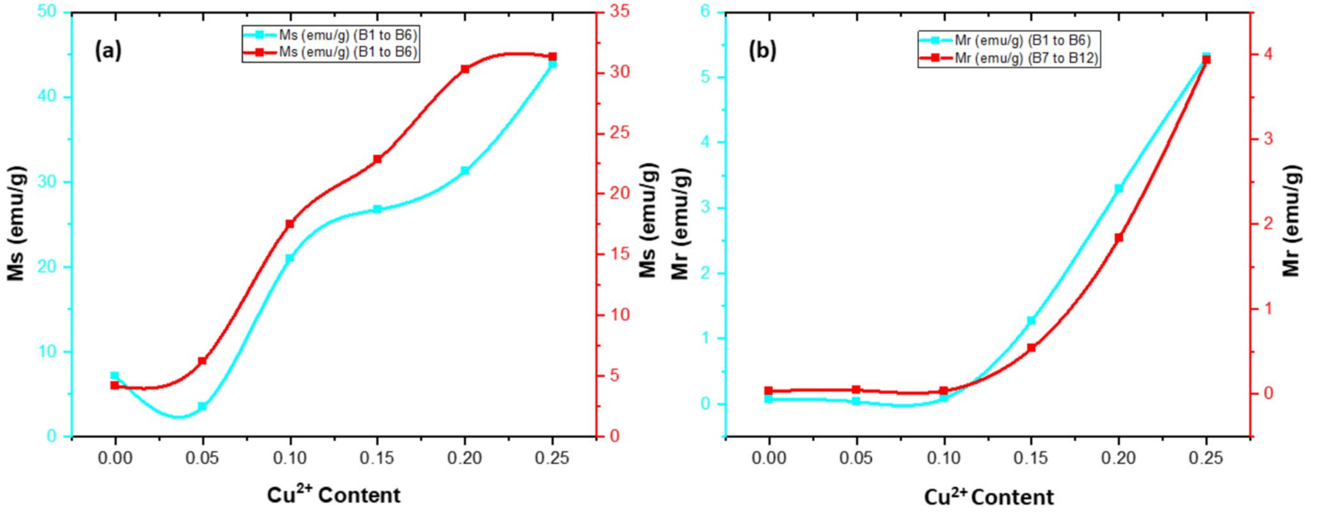

Fig. 7 Variation of M_s & M_r with Cu^{2+} for B1 to B12 Samples

behaviour for remanence (M_r). Behaviour of remanence (M_r) for samples B1 to B6 & B7 to B12 depicted in Fig. 7c. The augmentation of saturation magnetization and remanence with copper content in Mn–Zn spinel ferrites can be ascribed to alterations in the material's magnetic geometry and cation distribution resulting from the substitution of copper ions. In mixed ferrite spinel nanoparticles, Fe^{3+} cations exhibit A–B super exchange interactions. In addition, the Cu-concentration enhances the A–B exchange interaction between the A–B sublattices in Mn–Zn–Cu ferrite nanoparticles [43]. The observed increment in M_r and M_s may be caused due to increased strength of the A-B super exchange interaction [44, 45]. Variation in crystalline size observed in XRD studies could also be ascribed to variation in M_r & M_s values. As change in size elevates the magnetic ordering [18]. Generally, RE (like Gd^{3+}) ions have tendency to occupy B-site. Hence, the addition of RE is one of the reasons attributed for M_s reduction, as addition of RE in spinel ferrite is disturbing cation distribution. Hence, in B1 to B6 samples due to addition of Gd^{3+}, M_s initially reduced but with varied Cu^{2+} content effect of RE overcome by Cu^{2+} addition.

An experimental magnetic moment calculated using the relation,

$$\text{Magnetic moment}(\mu_B) = \frac{M_W \times M_s}{5585}, \tag{18}$$

where 5585 is a magnetic factor and M_W is molecular weight. Calculated values are presented in Table 3. The obtained value shown increment from 0.3 μ_B to 1.9 μ_B for B1 to B6 samples whereas 0.17 μ_B to 1.31 μ_B for B7 to B12 samples. This phenomenon is ascribed to direct dependence on saturation magnetization.

The squareness ratio (S) which provides insights into the magnetic behaviour of material merely depends on anisotropy of nanoparticles. The magneto-crystalline anisotropy and super exchange interaction of ferrites are reflected in the value of squareness ratio (M_r/M_s). It is a significant property in determining magnetic hardness of a material. Magnetic anisotropy, density, particle size, crystal defects, and synthesis methods all significantly influence the squareness ratio. The material is more anisotropic, hard, and single domain if the Squareness ratios are high ($0.5 < M_r/M_s < 1$). Furthermore, it is mentioned that SQR has value $0.05 < M_r/M_s < 0.5$ is for particles that interact with pseudo-single domain magneto-static couplings while $M_r/M_s < 0.05$ is for randomly oriented multi-domain magnetic nanoparticles [46]. Squareness ratio evaluated using the relation,

$$\text{Squareness ratio } (S) = \frac{M_r}{M_s} \tag{19}$$

Calculated values are presented in Table 5. The squareness ratio ranges from 0.009 to 0.120 for Gd^{3+} substituted samples and 0.007 to 0.125 for Gd^{3+} unsubstituted samples indicate the multidomain and pseudo single domain nature [47, 48].

4 Conclusion

Gadolinium substituted and unsubstituted spinel ferrite nanoparticles with varied Cu^{2+} concentration synthesized via co-precipitation approach. The crystalline nature of $Mn_{0.5}Zn_{0.5-x}Cu_xFe_{2-y}O_4Gd_y$ nanoparticles studied by X-ray diffraction technique. XRD data demonstrated the successful integration of Cu^{2+} and Gd^{3+} ions into the Mn–Zn spinel lattice. The distinct diffraction peaks observed at multiple angles validate the cubic spinel structure and indicate the Fd-3m space group of the spinel phase. The spectra of all samples obtained by Fourier Transform Infrared spectroscopy for functional group analysis in the range 400 to 4000 cm^{-1}. A significant absorption bands between 400 and 600 cm^{-1} range indicate and confirm the emergence of the spinel ferrite phase. SEM images confirmed the presence of nanoscale particles in all samples. EDS spectra confirmed the presence of all elements in synthesized samples as per expectancy. The physical characteristics and the size of spinel ferrite nanoparticles are analyzed using transmission electron microscopy (TEM). The bright zones in the SAED patterns illustrate the polycrystalline characteristics of the materials, supporting the XRD results. Room temperature magnetic characteristics revealed coercivity (Hc), saturation magnetization (M_s), and remanence (M_r) from the VSM observations. Samples that display an S-shaped curve demonstrated soft magnetic properties. Overall, the microstructure and magnetic characteristics can be considerably enhanced by adding a modest quantity of rare earth elements. Further research is needed to explore the mechanisms behind the observed improvements and to optimize doping strategies for various applications in the electronics industry.

Author contribution

All authors have equal contributions.

Funding

No funding.

Data availability

Data will be made available on request.

Declarations

Competing interests The authors declare that they have no known competing financial interests or personal relationships that could have appeared to influence the work reported in this paper.

References

1. S.M. Suryawanshi et al., Structural, surface, magnetic, and dielectric properties of Ni0. 3Cu0. 3Zn0. 4Fe1. 4Cr0. 6O4 spinel ferrite nanocrystals prepared by sol-gel auto combustion route. Inorg. Chem. Commun. **156**, 111204 (2023). https://doi.org/10.1016/j.inoche.2023.111204
2. K. Sharma et al., A review paper: synthesis techniques and advance application of Mn-Zn nano-ferrites. Mater. Today. (2023). https://doi.org/10.1016/j.matpr.2022.12.088
3. G. Kogias, V.T. Zaspalis, Temperature stable MnZn ferrites for applications in the frequency region of 500 kHz. Ceram. Int. **42**(6), 7639–7646 (2016). https://doi.org/10.1016/j.ceramint.2016.01.176
4. R. Lebourgeois, C. Coillot, Mn–Zn ferrites for magnetic sensor in space applications. J. Appl. Phys. (2008). https://doi.org/10.1063/12838994
5. A. Kumar, P.S. Rana, M.S. Yadav, R.P. Pant, Effect of Gd3+ ion distribution on structural and magnetic properties in nano-sized Mn–Zn ferrite particles. Ceram. Int. **41**(1), 1297–1302 (2015). https://doi.org/10.1016/j.ceramint.2014.09.060
6. Z. Hedayatnasab, F. Abnisa, W.M.A.W. Daud, Review on magnetic nanoparticles for magnetic nanofluid hyperthermia application. Mater. Des. **123**, 174–196 (2017). https://doi.org/10.1016/j.matdes.2017.03.036
7. M. Back, E. Trave, R. Marin, N. Marzocco, D. Cristofori, P. Riello, Energy transfer in Bi- and Er-Codoped Y2O3 nanocrystals: an effective system for rare earth fluorescence enhancement. J. Phys. Chem. A **118**, 30071 (2014)
8. M. Naeem, N.A. Shah, I.H. Gul, A. Maqsood, Structural, electrical and magnetic characterization of Ni–Mg spinel ferrites. J. Alloy Compd. **487**(1–2), 739–743 (2009). https://doi.org/10.1016/j.jallcom.2009.08.057
9. R. Mullai, P.P. Pradeep, G. Chandrasekaran, Synthesis and characterization of lanthanum doped Mg-Zn ferrite

nanoparticles prepared by sol-gel method. Int. J. Recent Trends Sci. Technol. **5**, 78–85 (2012)

10. Zhong, X. C., Guo, X. J., Zou, S. Y., Yu, H. Y., Liu, Z. W., Zhang, Y. F., & Wang, K. X. (n.d.). Improving soft magnetic properties of Mn-Zn ferrite by rare earth ions doping, https://doi.org/10.1063/1.4993645
11. S. Torkian, A. Ghasemi, R.S. Razavi, Structural and magnetic consequences of Mn 0.6 Zn 0.4 Fe 2–x Gd x O 4 ferrite. J. Supercond. Novel Magn. **29**, 1617–1625 (2016). https://doi.org/10.1007/s10948-016-3458-6
12. K. Tanbir et al., Gd-doped soft Mn–Zn nanoferrites: synthesis, microstructural, magnetic and dielectric characterizations. J. Mater. Sci. Mater. Electron. **31**, 3529–3538 (2020). https://doi.org/10.1007/s10854-020-02901-1
13. P. Thakur et al., Gd3+ doped Mn-Zn soft ferrite nanoparticles: superparamagnetism and its correlation with other physical properties. J. Magn. Magn. Mater. **432**, 208–217 (2017). https://doi.org/10.1016/j.jmmm.2017.01.081
14. R. Islam et al., Study of the structural, magnetic and electrical properties of Gd-substituted Mn–Zn mixed ferrites. J. Alloy Compd. **559**, 174–180 (2013). https://doi.org/10.1016/j.jallcom.2012.12.080
15. T.N. Brusentsova et al., Synthesis and investigation of magnetic properties of Gd-substituted Mn–Zn ferrite nanoparticles as a potential low-TC agent for magnetic fluid hyperthermia. J. Magn. Magn. Mater. **293**(1), 298–302 (2005). https://doi.org/10.1016/j.jmmm.2005.02.023
16. A. Shrivastava, A.K. Shrivastava, Effect of Gd doping on structural, morphological and magnetic properties of Mn-Zn soft ferrites nanoparticles (2021), https://doi.org/10.21203/rs.3.rs-500764/v1
17. A. Sharma et al., Investigation of dielectric, electrical and optical properties of copper substituted Mn-Zn nanoferrites. J. Mater. Sci.: Mater. Electron. **32**, 313–322 (2021). https://doi.org/10.1007/s10854-020-04782-w
18. N.I. Abu-Elsaad, A.S. Nawara, Effect of Cu substitution on magnetic and photocatalytic properties of Mn–ZnFe2O4 nanoparticles. J. Mater. Sci. **59**(10), 4167–4185 (2024). https://doi.org/10.1007/s10853-024-09486-8
19. F. Alam et al., Effect of Cu2+ on structural, elastic and magnetic properties of nanostructured Mn–Zn ferrite prepared by a sol-gel auto-combustion method. Physica B **594**, 412329 (2020). https://doi.org/10.1016/j.physb.2020.412329
20. T. Suneetha, G. Narayana Rao, T. Ramesh, Structural, vibrational and magnetic properties of Cu-substituted Mn0. 5Zn0. 5Fe2O4 nanoparticles. J. Mater. Sci. Mater. Electron. **32**(11), 14420–14436 (2021). https://doi.org/10.1007/s10854-021-06002-5
21. S.E. Jacobo, P.G. Bercoff, Structural and electromagnetic properties of yttrium-substituted Ni–Zn ferrites. Ceram. Int. **42**(6), 7664–7668 (2016). https://doi.org/10.1016/j.ceramint.2016.01.180
22. S.A. Mazen, H.M. Elsayed, N.I. Abu-Elsaad, Effect of divalent metal ions substitution on structural and magnetic properties of Li0.25Mn0.5-xMxFe2.25O4 (M=Co2+, Ni2+, Cu2+) spinel ferrites. Mater. Chem. Phys. **256**, 123676 (2020). https://doi.org/10.1016/j.matchemphys.2020.123676
23. S.A. Mazen et al., The effect of titanium on some physical properties of CuFe2O4. Phys. Status Solidi A **134**(1), 263–271 (1992). https://doi.org/10.1002/pssa.2211340123
24. A. Dinesh, K.K. Raja, A. Manikandan, M.A. Almessiere, Y. Slimani, A. Baykal, A. Khan, Sol–gel combustion synthesis and photocatalytic dye degradation studies of rare earth element Ce substituted Mn–Zn ferrite nanoparticles. J. Mater. Res. Technol. **18**, 5280–5289 (2022). https://doi.org/10.1016/j.jmrt.2022.04.121
25. P. Thakur, R. Sharma, V. Sharma, P.B. Barman, M. Kumar, D. Barman, S.C. Katyal, P. Sharma, J. Magn. Magn. Mater. **432**, 208–217 (2017). https://doi.org/10.1016/j.jmmm.2017.01.081
26. P. Thakur et al., A review on MnZn ferrites: synthesis, characterization and applications. Ceram. Int. **46**(10), 15740–15763 (2020). https://doi.org/10.1016/j.ceramint.2020.03.287
27. A. Aslam et al., To study the structural, electrical, and magnetic properties of M (M= Mg2+, Mn2+, and Cd2+) doped Cu-Ni-Co-La spinel ferrites. Mater. Chem. Phys. **294**, 127034 (2023). https://doi.org/10.1016/j.matchemphys.2022.127034
28. K.V. Zipare, S.S. Bandgar, G.S. Shahane, Effect of Dy-substitution on structural and magnetic properties of MnZn ferrite nanoparticles. J. Rare Earths **36**(1), 86–94 (2018). https://doi.org/10.1016/j.jre.2017.06.011
29. S.I. Ahmad, D.R. Kumar, I.A. Syed, R. Satar, S.A. Ansari, Structural, spectroscopic and magnetic study of nanocrystalline cerium-substituted magnesium ferrites. Arab. J. Sci. Eng. **42**, 389–398 (2017). https://doi.org/10.1007/s13369-016-2297-x
30. A.M. Moustafa, L.M. Salah, M. Salerno, M.H. Abdellatif, Symmetry in magnetic and vibrational spectra of multi-element spinel ferrite. J. Magn. Magn. Mater. **513**, 167267 (2020). https://doi.org/10.1016/j.jmmm.2020.167267
31. Daf, S. R., Badwaik, D. S., Suryawanshi, S. M., Harode, V. S., & Balbudhe, B. R. (2023). Physical, spectroscopic and antibacterial investigation of Mg0. 3Zn0. 5Mn0. 2Fe2O4 via temperature dependent hydrothermal approach.

Journal of Magnetism and Magnetic Materials, 567, 170346, https://doi.org/10.1016/j.jmmm.2022.170346

32. S. Li et al., Structure and magnetic properties of coprecipitated nickel-zinc ferrite-doped rare earth elements of Sc, Dy, and Gd. J. Mater. Sci. Mater. Electron. **32**, 13511–13526 (2021)
33. S.R. Naik, A.V. Salker, Change in the magnetostructural properties of rare earth doped cobalt ferrites relative to the magnetic anisotropy. J. Mater. Chem. **22**, 2740–2750 (2012). https://doi.org/10.1039/c2jm15228b
34. L. Zhao, H. Yang, X. Zhao, L. Yu, Y. Cui, S. Feng, Magnetic properties of CoFe 2 O4 ferrite doped with rare earth ion. Mater. Lett. **60**, 1–6 (2006). https://doi.org/10.1016/j.matlet.2005.07.017
35. K.B. Modi, N.H. Vasoya, V.K. Lakhani et al., Magnetic phase evolution and particle size estimation study on nanocrystalline Mg–Mn ferrites. Appl. Nanosci. **5**, 11–17 (2015). https://doi.org/10.1007/s13204-013-0287-9
36. H.F. Lu, R.Y. Hong, H.Z. Li, Influence of surfactants on co-precipitation synthesis of strontium ferrite. J. Alloy. Compd. **509**(41), 10127–10131 (2011). https://doi.org/10.1016/j.jallcom.2011.08.058
37. M.N. Akhtar, M.A. Khan, Effect of rare earth doping on the structural and magnetic features of nanocrystalline spinel ferrites prepared via sol gel route. J. Magn. Magn. Mater. **460**, 268–277 (2018). https://doi.org/10.1016/j.jmmm.2018.03.069
38. R.K. Panda, R. Muduli, D. Behera, Electric and magnetic properties of Bi substituted cobalt ferrite nanoparticles: evolution of grain effect. J. Alloys Compd. **634**, 239–245 (2015). https://doi.org/10.1016/j.jallcom.2015.02.087
39. H. Anwar, A. Maqsood, Enhancement of electrical and magnetic properties of Cd2+ doped Mn-Zn soft nanoferrites prepared by the sol-gel autocombustion method. J. Magn. Magn. Mater. **333**, 46 (2013). https://doi.org/10.1016/j.jmmm.2012.12.027
40. A. Iftikhar, M.U. Islam, M.S. Awan, M. Ahmad, S. Naseem, I.M. Asif, Synthesis of super paramagnetic particles of Mn1–xMgxF2O4 ferrites for hyperthermia applications. J. Alloys Compd. **601**, 116 (2014). https://doi.org/10.1016/j.jallcom.2014.02.138
41. B. Liu, D.K. Weller, "Heat assisted magnetic recording film including superparamagnetic nanoparticles dispersed in an antiferromagnetic or ferrimagnetic matrix." U.S. Patent 7,158,346, issued January 2, 2007.
42. A. Moser, K. Takano, D.T. Margulies, M. Albrecht, Y. Sonobe, Y. Ikeda, S. Sun, E.E. Fullerton, Magnetic recording: advancing into the future. J. Phys. **35**(19), R157 (2002)
43. F. Alam, M.L. Rahman, B. Chandra Das, A.K.M. Akther Hossain, Effect of Cu2? on structural, elastic and magnetic properties of nanostructured Mn–Zn ferrite prepared by a sol–gel auto-combustion method. Physica B **594**, 412329–412341 (2020). https://doi.org/10.1016/j.physb.2020.412329
44. C. Venkataraju, G. Sathishkumar, K. Sivakumar, Effect of Cd on the structural, magnetic and electrical properties of nanostructured Mn–Zn ferrite. J. Magn. Magn. Mater. **323**, 1817–1822 (2011). https://doi.org/10.1016/j.jmmm.2011.02.017
45. J. Slama, A. Grusková, M. Ušáková, E. Ušák, R. Dosoudil, Contribution to analysis of Cu-substituted NiZn ferrites. J. Magn. Magn. Mater. **321**, 3346–3351 (2009). https://doi.org/10.1016/j.jmmm.2009.06.024
46. M.A. Almessiere, Y. Slimani, M. Sertkol, M. Nawaz, A. Sadaqat, A. Baykal, I. Ercan, B. Ozçelik, Effect of Nb3+ substitution on the structural, magnetic, and optical properties of Co0.5Ni0.5Fe2O4 nanoparticles. Nanomaterials **9**, 430 (2019). https://doi.org/10.3390/nano9030430
47. S.S. Jadhav, S.E. Shirsath, B.G. Toksha, S.M. Patange, D.R. Shengule, K.M. Jadhav, Structural and electric properties of zinc substituted NiFe2O4 nanoparticles prepared by co-precipitation method. Physica B **405**(12), 2610–2614 (2010). https://doi.org/10.1016/j.physb.2010.03.008
48. P.M. Sontakke, S.R. Daf, D.S. Badwaik, S.M. Suryawanshi, A.V. Gongal, Structural and Magnetic investigation of Cu2+ substituted Mn-Zn spinel ferrite synthesized using hydrothermal route. Int. J. Architect. Eng. Constr. **11**(2), 61–73 (2022). https://doi.org/10.8845/52jxd453